A rocket-borne mass analyzer for charged aerosol particles in the mesosphere

Scott Knappmiller,[1,a)] Scott Robertson,[1] Zoltan Sternovsky,[1] and Martin Friedrich[2]

[1]*Laboratory for Atmospheric and Space Physics, University of Colorado, Boulder, Colorado 80309-0392, USA*
[2]*Institute of Communication Networks and Satellite Communications, Graz University of Technology, A-8010 Graz, Austria*

An electrostatic mass spectrometer for nanometer-sized charged aerosol particles in the mesosphere has been developed and tested. The analyzer is mounted on the forward end of a rocket and has a slit opening for admitting a continuous sample of air that is exhausted through ports at the sides. Within the instrument housing are two sets of four collection plates that are biased with positive and negative voltages for the collection of negative and positive aerosol particles, respectively. Each collection plate spans about an order of magnitude in mass which corresponds to a factor of 2 in radius. The number density of the charge is calculated from the current collected by the plates. The mean free path for molecular collisions in the mesosphere is comparable to the size of the instrument opening; thus, the analyzer performance is modeled by a Monte Carlo computer code that finds the aerosol particles trajectories within the instrument including both the electrostatic force and the forces from collisions of the aerosol particles with air molecules. Mass sensitivity curves obtained using the computer models are near to those obtained in the laboratory using an ion source. The first two flights of the instrument returned data showing the charge number densities of both positive and negative aerosol particles in four mass ranges. © *2008 American Institute of Physics.* [DOI: 10.1063/1.2999580]

I. INTRODUCTION

The summer polar mesosphere contains icy aerosol particles that may grow to become noctilucent clouds (NLCs).[1,2] The subvisual precursor particles modulate the electron density in the D region of the ionosphere and create radar backscatter known as polar mesosphere summer echoes (PMSE).[3] The ice particles are thought to nucleate on meteoric dust particles.[4] Several rocket-borne probes have been developed for *in situ* detection of the meteoric condensation nuclei and the icy particles responsible for NLC and PMSE. A significant fraction of these particles are likely to be charged in the ionospheric plasma and their charge provides a means for their detection. Rocket-borne probes measure charge deposited on an exposed collecting surface due to the impacting particles. Several Faraday cup-type instruments have been flown in which the charge is collected at the bottom of the instrument[5–7] or at the payload surface.[8] There is often a set of biased grids in front of the collecting plate to prevent light plasma particles from reaching the collection surface and to reduce or monitor charge that may be created by the impacts. The Gerdien condenser is a charge collector with a bias voltage that is scanned in time to vary the collected mass range.[9] An alternate design uses a magnetic field to prevent electron collection.[10–14] UV flashlamps have been incorporated into some instruments to measure changes in charge collection caused by photoionization and photoelectric charging of up-

stream particles.[15,16] All rocket-borne instruments are affected by the aerodynamic flow. A shock wave surrounding the payload may prevent or significantly reduce the collection efficiency for small particles. Also, the particles can be collisionally heated in the shock and sublimate.[17] These instruments have been single-channel instruments which give the charge density of the particles in the detected range of mass.

We describe an eight-channel instrument, the mesospheric aerosol sampling spectrometer (MASS), which uses electrostatic deflection to separate particles by their charge-to-mass ratio. The analyzer is mounted on the forward end of a rocket payload and has an entrance slit that admits a continuous sample of air that is exhausted at side windows. There are four electrically biased plates collecting positively charged particles and four plates collecting negatively charged particles. The electrostatic deflection voltages are designed so that the channels record the collected current for particles with the density of ice having radii of <0.5, $0.5–1$, $1–2$, and >3 nm. The currents are converted to charge densities using the rocket velocity, the area of the inlet slit, and the computed collection efficiencies. The instrument has been flown twice and returned data for the densities of positive and negative aerosol particles from both the uplegs and the downlegs of the flights. The mechanical and electrical designs are described in Sec. II below. Extensive numerical simulations that find the mass sensitivity of each channel are described in Sec. III and are compared with laboratory mea-

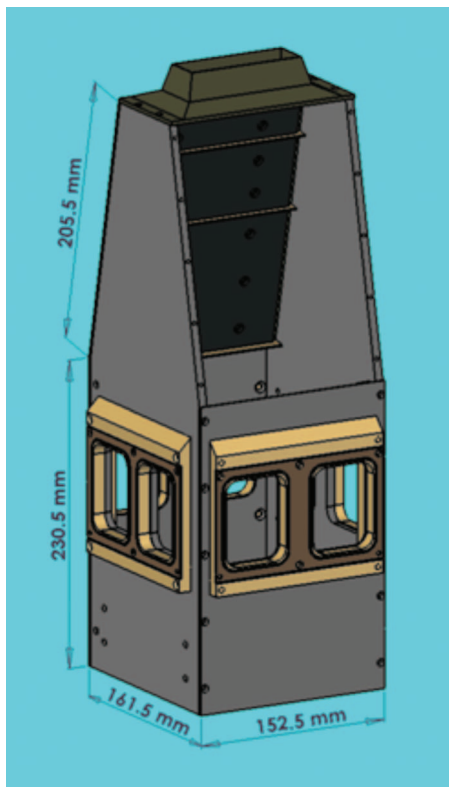a)Electronic mail: scott.knappmiller@colorado.edu.

FIG. 1. (Color) Mechanical drawing of the instrument. A panel and a set of graphite collecting plates have been removed to show the graphite collecting plates on the opposite side of the instrument.

surements. In Sec. IV, data from the upleg of the first flight are presented that show operation largely as expected. Section V is a short summary and conclusion.

II. INSTRUMENT DESIGN

A. Mechanical

The instrument (Fig. 1) is mounted on the center of the forward payload deck so that it is directly exposed to the airflow. The air is sampled through a rectangular opening at the top of the payload and the opening geometry is optimized for particle collection in the aerodynamic flow. Within the instrument, the biased collection plates slope away from the opening to eliminate impacts from neutral aerosol particles and from the larger charged particles that have only a small deflection. Below the biased collection plates is a set of eight air exit windows to reduce stagnation.

The housing and mechanical support structure for the collection surfaces is made of aluminum for convenience. The instrument housing has a cross section of 153×162 mm^2 at the base. The overall height is 462 mm. The top 231 mm of the instrument slopes on two sides to a rectangular opening. This 28×90 mm^2 aperture with knifelike edges defines the entrance of the instrument. The area of the aperture is several times larger than the area of our previous dust impact detectors.[12] This change was made to increase the charge collected because the signal would be divided among eight collecting surfaces.

The collection surfaces are of graphite which has a low photoelectric yield.[18] This choice minimizes spurious cur-

rents due to solar ultraviolet radiation entering the instrument. The graphite is mounted on plastic insulating spacers of noryl, selected for its low moisture absorption. In order to provide a deflecting field that is uniform along the length of the slit, the graphite plates span the full inside width of the housing (140 mm) and are thus wider than the stream of aerosol particles (90 mm). The collection surfaces are separated by grounded brass spacers that help to shape the electric field distribution. Without these spacers, the collecting plates with the highest bias (± 54 V) would attract all light charged particles.

B. Electrical

The currents to the collection plates are measured by electrometers with a sensitivity of 1 V/nA. This gain was found to be appropriate in earlier flights of the dust impact detectors. The gain is obtained by using operational amplifiers with a 10 MΩ feedback resistance in combination with a 100 times voltage divider at the output of the op-amp. This combination circumvents the need for a 10^9 Ω feedback resistor which would create large time constants because of stray capacitance. The gains were calibrated before the flight using a precision resistor and voltage source. The first pair of collection plates is operated with an additional gain channel of 0.1 V/nA in order to avoid saturation by ions or electrons. Each channel includes a buffer amplifier to drive the signals to telemetry. The telemetry channels have an input range of 0–5 V; thus, an offset of 2.5 V is added to the signals so that either sign of current can be recorded. The offset is subject to small drifts of the order of 20 mV from changes in temperature and battery voltage; hence, the value used for each channel in the data analysis is taken from an average of the telemetry data over 1 s before the nosecone is deployed. The resolution of the digitizers is 12 bits; thus, a single digitizer step corresponds to a current of 1.25 pA. The root-mean-square noise level of the amplifiers is 3 pA when sampled at the telemetry rate of 1 kHz without an antialias filter. The noise bandwidth of the data is limited by a low pass filter with a 640 Hz cutoff frequency located after the current-to-voltage amplifier.

C. Sampling slit and exit windows

Numerical simulations[14,16,17] have shown that nanometer-sized particles are strongly affected by the shock wave of the payload and can be carried around the entrance of the instrument. The MASS design prevents the formation of a shock above the entrance slit. The opening is designed with a sharp edge ($\theta = 12°$ slope) that removes the shock immediately above the sampling slit. The condition for preventing a shock is $M \sin(\theta) < 1$, where M is the Mach number of the flow.[19] For typical atmospheric conditions in the mesosphere and a rocket velocity of 1000 m/s, this condition is satisfied. In the absence of a strong shock, the air slows more gradually and the slowing occurs within the instrument. The pressure buildup within MASS is reduced by two venting windows on each of the four sides of the instrument housing. The size and location of the windows were determined using numerical flow simulations with the DSMC

method.[20] The simulated volume included the 36 cm diameter forward bulkhead below the instrument. It was found that placing the windows 11 cm forward of the bulkhead avoided disturbances to the flow caused by the bulkhead. The total window area is 260 cm^2, which is an order of magnitude greater than the area of the entrance slit.

The venting windows are covered by a screen mesh with 80% transparency. This mesh is biased at -10 V in order to prevent electrons and light ions from entering the instrument as a consequence of their high thermal speed and thus contributing to the collected current. This negative bias potential was selected to be much larger than any charging potential that might occur on the rocket payload. Ions, on the other hand, are collected on the wires of the mesh. The theory of cylindrical wire probes in plasmas[21] shows that the effective cross section of the wire is increased by the factor of $(1-q\Phi/\kappa T)^{1/2}$, where q is the ion charge, Φ is the potential on the wire, κ is Boltzmann's constant, and T is the charged particle temperature (assumed to be the 140 K in the mesopause region). The grid is chosen so that the spacing between grid wires, 1.2 mm, is less than the radius of the effective cross section, 1.4 mm.[22]

III. NUMERICAL AND LABORATORY CALIBRATION PROCEDURES

A numerical simulation is used to find the range of masses collected on each electrode by calculating the trajectories of the charged aerosols in MASS including the Coulomb force and the impulsive forces from collisions with the air flow field. The trajectory simulation requires the results from two additional computer simulations as inputs. The first code finds the electric field within the instrument and the second finds the air flow field. The MASS instrument is similar to the differential mobility analyzer in which an electric field is used for mass-selective separation of atmospheric aerosols.[23] In these instruments, the trajectories of the particles are calculated from the electric mobility and analysis is simplified by a constant air flow velocity. Our numerical simulations use a Monte Carlo approach to find the trajectories of the charged aerosols instead of electric mobility since the coefficients for electric mobility and drag that are calculated for an infinite homogeneous medium are not applicable when the mean free path is not small in comparison with the size of the instrument. For the smallest particles (light molecular ions and cluster ions), the mean free path within the MASS instrument is $\sim$1 cm at 90 km. Furthermore, the particle trajectories are complicated by the inhomogeneous air flow velocity, which varies from 0 to 1000 m/s within the MASS instrument.

A. Calibration by numerical simulation

1. Electric field

The deflecting electric field within the instrument is found from the gradient of the electrostatic potential. The potential is found using a numerical routine that solves Laplace's equation as a boundary value problem on a three-dimensional grid using the standard relaxation method.[24] A rectangular grid $(1 \times 2.5 \times 2.5 \text{ mm}^3)$ is defined with the
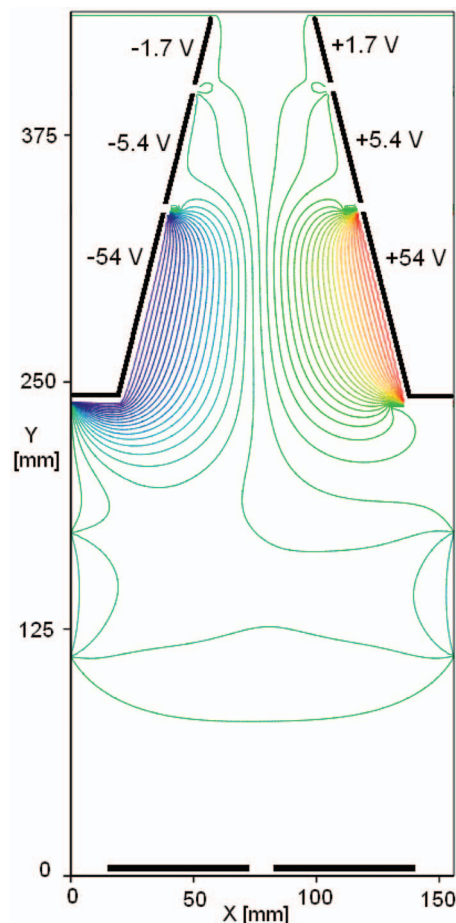

FIG. 2. (Color) Contours of the potential within the instrument at the midplane perpendicular to the collection plates. The contours extend from $+54$ V (red) to -54 V (blue).

highest resolution along the direction of the electric field. Boundary values for the potential are 0 V for the grounded surfaces, ±1.7, ±5.4, and ±54 V for the collecting surfaces, and -10 V for the grids covering the air exit windows. The potential profile for the plane in which the particles are deflected is shown in Fig. 2. The potential profile is not perfectly antisymmetric about the axis because the bias potential on the window exit grids is symmetric. The bias potential on the window exit grids creates a weak internal electric field and has negligible effect on the trajectories of the aerosol particles.

2. Aerodynamic flow

Flow simulations are performed using a commercial direct simulation Monte Carlo (DSMC) code.[19] A three-dimensional version of the code is used in which the instrument housing can be represented as a set of solid surfaces. The modeled surfaces include the cutouts for the entrance slit and exit windows. There is an insufficient spatial resolution to include the window grids. The simulation volume begins 82 mm upstream of the instrument and ends after the bulkhead. Preflight simulations were done to aid in the design using a nominal rocket speed of 1000 m/s. The simulations shown here were made postflight using the measured rocket speed that decreased from 1092 to 1000 m/s in the region of
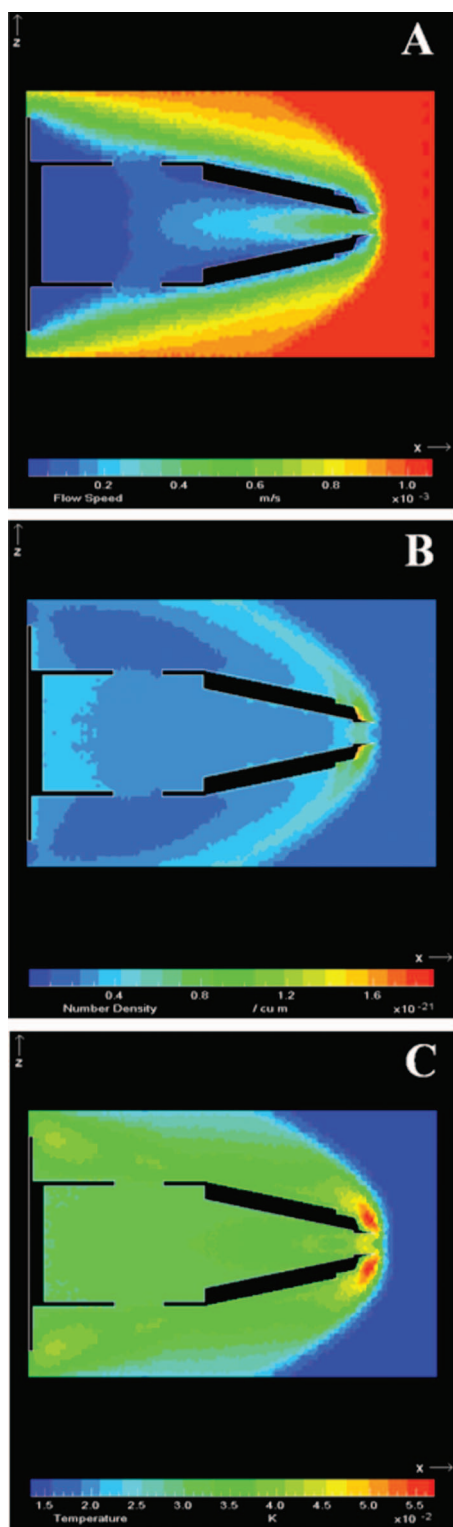
FIG. 3. (Color) (a) Flow velocity, (b) number density, and (c) temperature of the air within the MASS instrument from the DSMC code for conditions at 85 km.

interest. The upstream air temperatures and densities are taken from Lübken[25] using an interpolation to obtain values for the launch date. Simulations were done at altitudes of 80–90 km at 2.5 km intervals.

The simulations show that the change in the air speed at the entrance of MASS is less abrupt if the opening has a knifelike edge. The flow velocity [Fig. 3(a)] decreases gradu-

ally to zero at the bottom of the instrument. At 85 km altitude, the stagnant air at the bottom has a number density [Fig. 3(b)] that is about 1.5 times higher than the ambient density. The flow speed at the exit windows has some altitude dependence and is typically ~120 m/s which is much smaller than the rocket speed.

3. Particle trajectories within the instrument

The aerosol particle trajectories are found by integrating their equations of motion. The electric acceleration is found from $q\vec{E}/M$, where unit charge q is assumed, $\vec{E}$ is the electric field vector, and M is the mass of the aerosol particle. The effect of collisions is included using a Monte Carlo method adapted from Robertson and Sternovsky.[26] The physical principles involved in the aerodynamic slowing of subsonic aerosol particles were discussed by Epstein.[27] The supersonic case was discussed by Hayes and Probstein[28] and Probstein.[29] In developing the Monte Carlo model for the slowing, we use Epstein's assumption for his case 4b in which the incident molecule sticks to the particle surface and is subsequently emitted randomly. Epstein[27] did not consider the possibility of particle rotation, thus the molecules leaving the surface in his model have their velocity vectors limited to the 2π sr above the surface on which they landed. We assume that the exiting molecule is emitted randomly into 4π sr as a consequence of particle rotation. The emission process therefore has no preferred direction and does not result in slowing.

Let m be the mass of the air molecule, $\vec{u}_{in}$ be the velocity of the incident air molecule, and $\vec{u}_{ex}$ be the velocity of the emitted air molecule. Let $\vec{V}_0$ be the initial velocity of the aerosol particle, $\vec{V}_1$ be the velocity after the incident molecule has hit, and $\vec{V}_2$ be the velocity of the aerosol particle after emission of the incident molecule. Conservation of momentum for the first and second parts of the collision is

$$M\vec{V}_0 + m\vec{u}_{in} = (M+m)\vec{V}_1, \tag{1}$$

$$(M+m)\vec{V}_1 = M\vec{V}_2 + m\vec{u}_{ex}, \tag{2}$$

and for the complete collision

$$M\vec{V}_2 = M\vec{V}_0 + m(\vec{u}_{in} - \vec{u}_{ex}). \tag{3}$$

The problem is formulated in the rest frame of the instrument. The velocity of the incident air molecule in the rest frame of the gas is found by randomly choosing the three components of the velocity from a Maxwellian distribution (at the local temperature) using the rejection method.[25] The molecular mass is assumed to be 29 amu.[30] The velocity $\vec{u}_{in}$ is found by adding the air flow velocity to the selected random velocity. The velocity of the emitted air molecule is assumed to be random in the frame of the aerosol particle; thus, the velocity $\vec{u}_{ex}$ is found in the rest frame of the instrument by selecting a random velocity and adding the velocity of the aerosol particle $\vec{V}_1$ after the first half of the collision. If $\vec{u}_r$ is a velocity chosen randomly from a Maxwellian distribution and $\vec{u}_i$ is the flow velocity of the distribution, then the effect of the collision can be reduced to

$$\vec{V}_2 = \vec{V}_0 + \left(\frac{m}{M}\right)(\vec{u}_r + \vec{u}_i - \vec{u}_r - \vec{V}_1). \tag{4}$$

The velocity of the aerosol particle is changed by the prescription in Eq. (4) at each collision. For a subsonic velocity, the collision frequency ν_{sub} is found from the surface area of the aerosol particle (assumed spherical) and the random flux of molecules to a surface,

$$\nu_{sub} = 4n\pi r^2 \sqrt{\frac{\kappa T}{2\pi m}}, \tag{5}$$

where n is the number density of air molecules. The radius r of an aerosol particle with mass m is calculated assuming a spherical particle of ice with density of 931 kg/m^3. This assumption ignores the condensation nuclei that may have greater density. For supersonic relative velocity, the molecules are incident on one side of the aerosol particle and the cross section in projection is used,

$$\nu_{sup} = n\pi r^2 U = n\pi r^2 |\vec{V}_0 - \vec{u}_i|. \tag{6}$$

In the transition region between subsonic and supersonic, an approximate collision frequency is found by adding these two collision frequencies in quadrature,

$$\nu_0 = \sqrt{\nu_{sub}^2 + \nu_{sup}^2}. \tag{7}$$

In the computer code, time steps dt are taken which are much smaller than the mean time between collisions. A collision is made if a number chosen randomly on the domain [0, 1] are smaller than $\nu_0 dt$ and the velocity of the aerosol particle is changed using Eq. (4).

The code was tested in the subsonic limit against the analytical expressions for the slowing of particles given by Epstein.[27] In the subsonic limit, the computed slowing time is found to be about a factor of 2 longer than Epstein's slowing time because the emission of the molecule has no preferred direction in our model that assumes particle rotation.

Simulated trajectories of aerosol particles within the instrument are shown in Fig. 4 for several of the masses used in the simulations. The starting grid is above the shock, 82 mm above the instrument opening and thus the particles are followed through the shock. The aerosol particles are given starting velocities that are the upstream flow speed plus a random thermal speed that is dependent on the mass and the upstream temperature. The masses in the simulations are spaced logarithmically by factors of $\sqrt{2}$ and span $30-1.3 \times 10^6$ amu, a total of 35 different mass values. This simulation is split into small particles (<1000 amu) and large particles (>1000 amu). For the larger masses, 80 particles are followed having starting positions that are on a uniform grid with eight points across the shortest dimension of the opening and ten points along the longest dimension. The points along the longest dimension are between the center of the opening and one side. Trajectories in the other half of the instrument would be the same because of symmetry.

The smallest mass used in the simulations, 30 amu, corresponds to the lightest common ion in the mesosphere, NO^+. In addition, masses of 55, 73, 91, and 109 amu are used for the proton hydrates with 3, 4, 5, and 6 monomers. For the
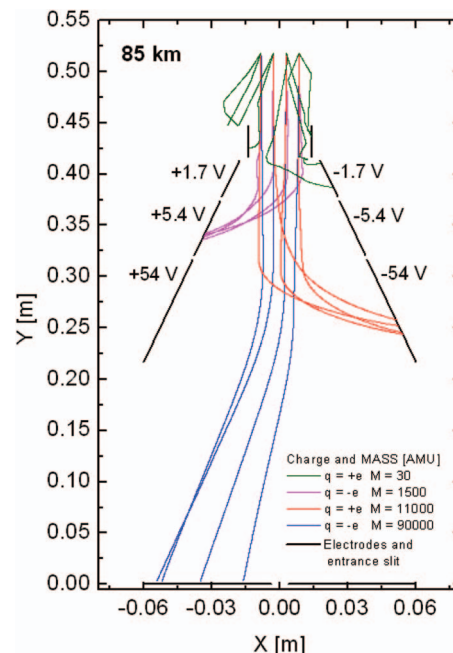

FIG. 4. (Color) Computer simulation of the trajectories of particles within the instrument for masses selected to fall on each of the collection plates. A total of four masses is shown with alternating polarity. A large fraction of the 30 amu particles are lost to the wall before collection. The 1500 amu particles show some jitter in their trajectories as a result of collisions with gas molecules.

proton hydrates and the NO^+ ions the collision cross sections are taken from Sternovsky et al.[31] and Viehland et al.[32]

The lighter particles (30–1000 amu) have thermal velocities that are non-negligible and the trajectories deviate significantly from streamlines. There is scattering of these ions both into and out of the flow stream from collisions. In order to properly account for scattering into the flow stream, the starting grid for these ions is extended one slit width to either side of the grid directly upstream. The collection efficiency is defined as the number of particles falling on a collection plate divided by the number of particles with trajectories started in the volume directly upstream of the slit. A total of 806 particle trajectories is followed for each mass below 1000 amu and 198 of those particles are directly above the entrance of the instrument.

The trajectories of the heaviest particles are smooth because each collision has a small effect. These collisions cannot be ignored, however, because their cumulative effect is a significant slowing which increases the deflection by the electric field and thus shifts the range of mass that is detected. The deflection has a slight focusing effect on the particles collected by the second and third collection plates. The focusing is most evident for the 1500 amu particles in Fig. 4. The footprint of these particles on the collecting plate is significantly smaller than the width of the slit as a result of the focusing.

4. Calibration curves from simulation

The fraction of the starting particles that are collected is plotted in Fig. 5 for each mass and each collection plate at altitudes of 80 and 90 km. The calibration curves have been
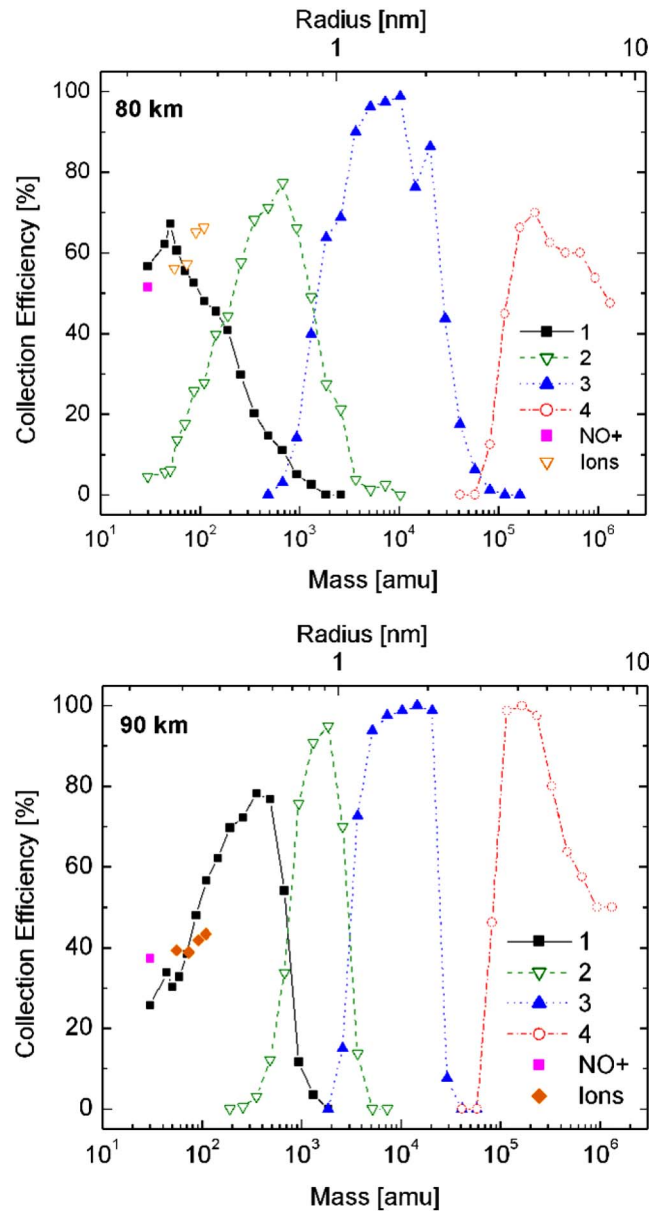
FIG. 5. (Color online) Calibration curves for the four collection plates in the instrument determined by the computer modeling for altitudes of 80 and 90 km. The numbers refer to the collection plate locations, with 1 being nearest to the opening. The gap in collection near 40 000 amu is a consequence of the space for the exit windows. The points labeled ions are the calibration points on the first (second) plate at 90 km (80 km) for the water cluster ions (proton hydrates) with masses of 55, 73, 91, and 109 amu. The point labeled NO$^+$ is for collection on the first plate for both 80 and 90 km.

labeled with both mass and particle radius. The collection efficiency of the first collection plate is ∼26% at the low end of its mass range at an altitude of 90 km. Plots of the trajectories (Fig. 4) show that at 85 km the thermal velocities of the lightest particles carry a significant fraction into the sides of the detector before they reach the collection plates, thus accounting for the low collection efficiency for small masses. The second and third collection plates have collection efficiencies nearer to 100% at the centers of their mass ranges. The ranges of mass collected are shown in Table I for altitudes of 80 and 90 km. The ends of the mass ranges are defined as the masses for which the sensitivity is half that of the maximum. The effect of the larger atmospheric density at 80 km is to increase the number of collisions, which widens the range of masses collected on each plate. This effect is most visible for collection plates 2 and 3 in Fig. 5. The increase in collisions has a large impact on the proton hydrates as their collision cross section is approximately three times as large as a spherical ice particle with the same mass. As a result, the proton hydrates collection is shifted from the first plate at 90 km to the first and second plate at 80 km (Fig. 5). The collection at 80 km is dominated by the second plate as the proton hydrates trajectories are more fixed to the velocity flow field. In contrast, the NO$^+$ ion is negligibly affected by the increase in density at 80 km due to its collision cross section being approximately two times smaller than a spherical ice particle with the same mass. In consequence, NO$^+$ is collected on the first plate for both 80 and 90 km.

The fourth set of collection plates is at the bottom of the instrument (see Fig. 2) and these plates collect particles that have small deflection. The plates are separated by a 7 mm gap that allows some undeflected charged particles to escape detection. At the highest masses simulated (∼1×10^6 amu), the collection efficiency is reduced to ∼0.5 because of particles falling into the gap between plates. In the limit of zero deflection or very large mass the collection efficiency of the fourth plate becomes 37.5%, which is the ratio of the area of the collection plate directly below the opening of the mass instrument to the opening of the instrument.

5. Effect of payload potential

Rocket payloads in the mesosphere often acquire negative potentials of the order of −1 V relative to the ambient plasma.[33] This potential is not negligible in comparison with the voltages on the collection plates and thus can alter the collection efficiency curves. This effect was investigated by adding a potential drop of −1 V with a uniform gradient over a 1 cm distance above the entrance to the instrument.

TABLE I. Range of masses detected by each of the four collection plates obtained by numerical simulations for conditions at 80 and 90 km. Columns 2 and 3 are with no rocket potential. Columns 3 and 4 are with −1 volt potential for positively charged aerosols and columns 5 and 6 are for negatively charged aerosols. The final column is the mass ranges from the laboratory calibration.

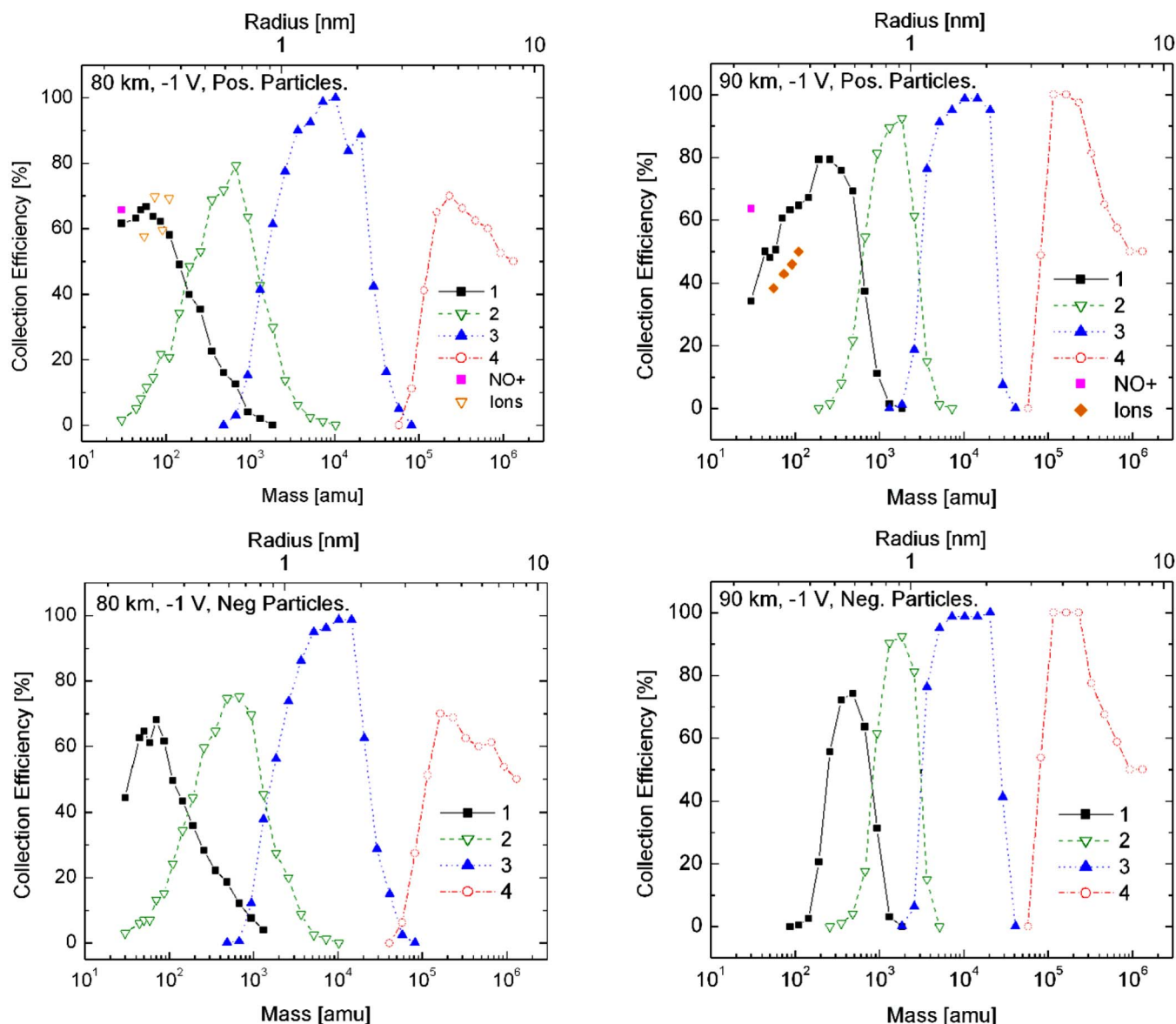| Plate No.	80 km	90 km	80 km (+) −1 V	90 km (+) −1 V	80 km (−) −1 V	90 km (−) −1 V	Laboratory
1	<200	70–800	<300	35–600	<250	200–900	
2	200–1500	800–3000	180–1500	600–3000	160–1500	900–3000	300–2000
3	1500–30 000	3000–25 000	1500–30 000	3000–25 000	1600–22 000	3000–28 000	2000–20 000
4	>50 000	>85 000	>95 000	>80 000	>90 000	>90 000	>60 000

FIG. 6. (Color online) Calibration curves calculated with an external electric field above the instrument to simulate the payload charging to −1 V.

The distance was chosen to be approximately the Debye length in conditions without NLC and PMSE. At 80 km (Fig. 6), the payload potential has a negligible effect due to the greater atmospheric density and hence more collisions. However, as the atmospheric density decreases the payload potential has a larger affect. The primary result of −1 V payload potential on the calibration curves at 90 km (Fig. 6) is that negatively charged aerosols with $m < 200$ amu are not collected. Small negatively charged aerosols from 200 to 500 amu have their collection efficiency decreased. The increase in collection efficiency for aerosols from 500 to 1000 amu on the first collection plate is from particles that would have fallen on the second collection plate in the absence of the −1 V potential. Electron collection was not simulated because of the small electron mass. However, from the effect on light negative ion collection it can be deduced that electrons would not be collected. The positive aerosol particles at 90 km have their collection efficiency increased (by about

20%) for masses between 30 and 1000 amu and particles with masses greater than 1000 amu are nearly unaffected.

B. Laboratory calibration

A preflight mass calibration and a flight-readiness test were performed in the laboratory using argon ions that were accelerated to the same energy that an incident aerosol particle would have at the nominal rocket velocity. Time constraints did not permit completion of the numerical simulations until after the launch. The deflection of the incoming particles depends on their incident kinetic energy divided by their charge. The aerosol particle kinetic energy is determined by the particle mass and the rocket velocity, thus the particle mass can be deduced from the deflection if the rocket velocity and the particle charge are known. The calibration curves for the argon ions as a function of energy are converted to calibrations for aerosol particle mass using a rep-
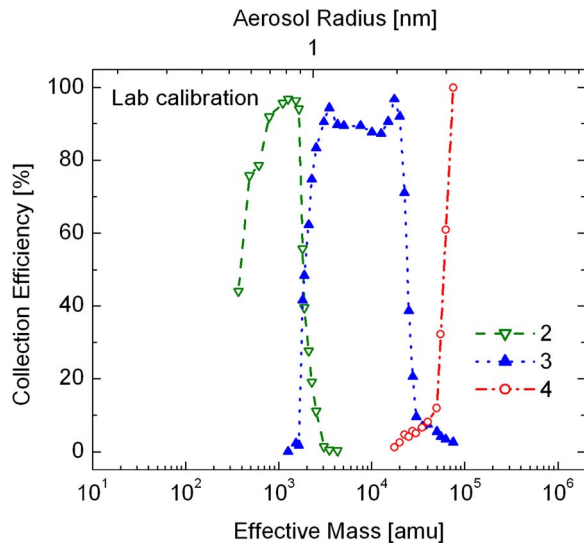
FIG. 7. (Color online) Calibration curves obtained experimentally using argon ions with the same energy as aerosol particles incident at 1000 m/s. The numbers refer to the collection plate locations.

resentative rocket velocity of 1000 m/s and an assumed single charge on the aerosol particle. This instrument test was performed because the numerical simulations could not be completed before the launch.

The ion source is a radio-frequency source.[34] Ions are extracted from argon plasma and focused by an electrostatic lens. A movable gridded Faraday cup is used to measure the ion beam current and to verify the ion energy distribution. Typical beam energy ranges from 20 to 200 eV at a pressure of 10 mTorr. The mean free path is of the order of the vacuum chamber dimensions, which implies that the laboratory calibration is collisionless. An argon calibration for the first collection plate could not be obtained because of insufficient ion current at very low acceleration voltages. The ion source calibration curves for the second, third, and fourth pairs of collection plates are shown in Fig. 7 and the mass ranges are shown in Table I.

IV. FLIGHT PERFORMANCE

The first flights of two identical instruments were conducted from the Andøya Rocket Range, Norway, on 3 August 2007 at 22:51 UTC and 6 August 2007 at 22:56 UTC as a part of an international effort investigating NLCs and associated radar echoes. The rocket apogees were approximately 133 km. The data from the upleg of the first flight are analyzed here to determine if the instrument operated as expected, to identify sources of spurious currents that might affect the quality of the data, and to uncover weaknesses in the design that could be corrected on future flights. The data from the downleg were similar. The second flight was into a weaker cloud and the signals were smaller. The rocket was pointed in the ram direction by an attitude control system and rotated at 2 Hz for stability. It was known from ground-based lidar and a rocket-borne photometer that NLC particles were in the region of 81–87 km at the time of launch.
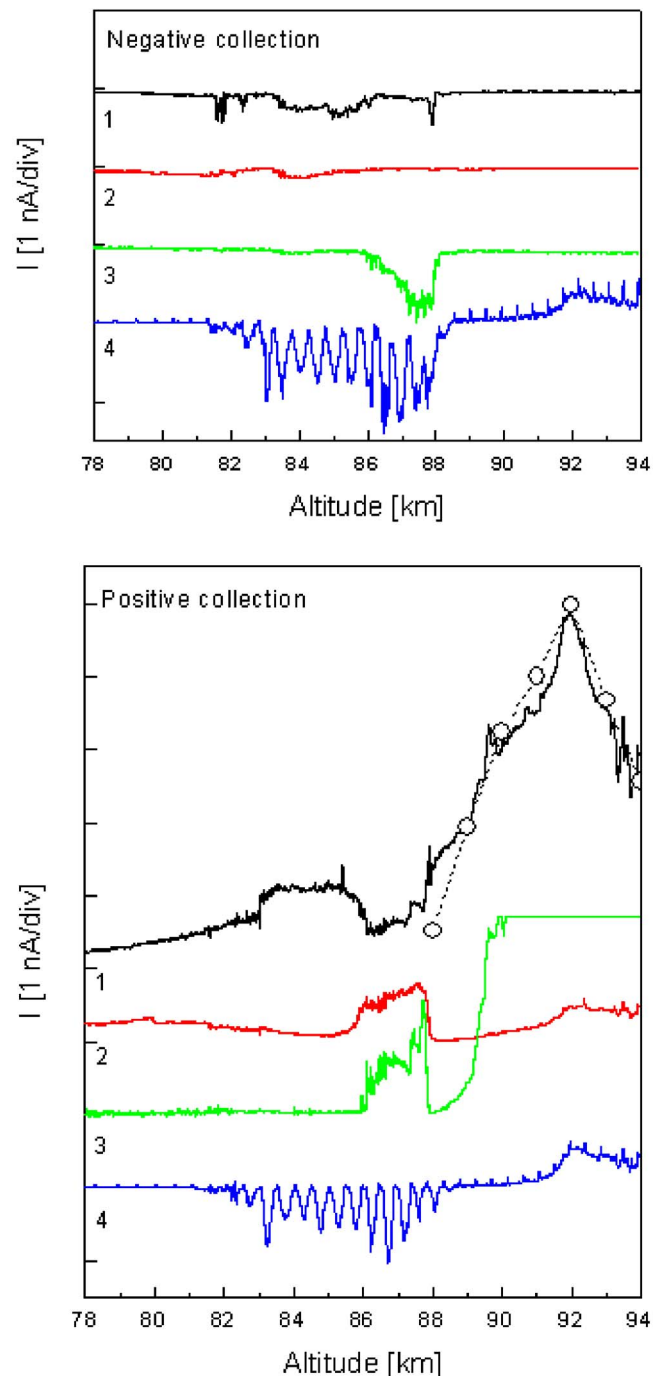

FIG. 8. (Color online) Signals from the four channels for negative charge (top panel) and signals from the four channels for positive charge (bottom panel). In the bottom panel, channel 4 collects negative charge because the heaviest particles are not significantly deflected. The circles show 0.6 of the electron density from Faraday rotation. The signals have been offset from one another by 1 nA for clarity.

A. Aerosol particle detection

Each of the eight channels of the instrument returned data (Fig. 8). The data were digitized at a 1 kHz rate which corresponds to 1 m resolution at the nominal rocket speed of 1 km/s. In order to reduce high-frequency noise, consecutive points were averaged using a Gaussian window with a width of 10 ms. The polarities of the signals indicate that the three positively biased plates collected negative charge and the

three negatively biased plates collected positive charge. The collected current I is related to the number density of charge by $I = fnqvA$, where n is the number density, v is the rocket velocity, A is the slit area, and f is the collection efficiency, thus a current of 1 nA corresponds to a charge number density of 2340 cm^{-3} if the collection efficiency is 100%.

The negatively biased plate No. 1 is expected to collect the lightest ions. The ion density should be equal to the electron density above the cloud, where electrons have not been scavenged by the cloud particles and negative ions are not expected. The dominant ion at this altitude is NO$^+$. Below the cloud, the ions may be proton hydrates with a wide range of masses.[35] Comparison of the ion density to the electron density (shown in Fig. 8) from a Faraday rotation instrument[36] on the same rocket shows that the ion density "tracks" the electron density from 88 to 94 km but is approximately 0.6 as large assuming a collection efficiency of 100%. The collection efficiency for NO$^+$ from the numerical simulations with −1 V rocket potential at 90 km is 0.64 and is 0.34 for spherical particles of ice (Fig. 6).

The positively biased collection plate No. 1 that could collect electrons has a signal much smaller in magnitude than would be consistent with the Faraday rotation measurement of electron density at 88–94 km. The small amplitude of the signal in this altitude range is consistent with there being a negative rocket potential that prevents electron collection. From 82 to 88 km, the Faraday rotation indicates a "bite-out" (reduction) in electron density from attachment of the electrons to the cloud particles thus an electron signal comparable to the ion signal is not expected at these altitudes.

The negatively biased collection plate No. 2 collected positive aerosol particles near the top of the cloud layer. The positively biased plate No. 2 showed a much smaller signal indicating the near absence of negatively charged particles in the mass range. The simulations show that the effect of a negative rocket potential is negligible at low altitudes and shifts the detected range of mass at high altitudes rather than to prevent detection completely (Table I).

The pair of collection plates No. 3 collected both positive and negative aerosol particles in the 1–2 nm range at the top of the cloud layer, 86–88 km. The negatively biased plates collected more than 2.5 nA above 88 km and the electronics became saturated. These plates are located adjacent to the venting windows. This saturation may be due to the collection of ions that have "leaked" through the biased window grids at higher altitudes.

The two unbiased collection plates (No. 4 in the figures) at the bottom of the instrument, designed to collect the largest particles (>3 nm), each collected negative charge. The signals from the two plates being of the same magnitude indicate that these particles were too massive to be significantly deflected. NLC particles are known from lidar measurements to grow to ∼50 nm radius;[37] thus, the signals are consistent with the presence of a cloud from 81 to 88 km. The signals to the bottom plates were modulated at the rocket spin rate of 2 Hz, indicating that the aerosol particles entered with a velocity vector slightly misaligned with the rocket axis. This may be a result of a horizontal wind or inaccuracy in the attitude control system.

B. Microphonic noise

Flight data showed unanticipated microphonic noise at the times of the firings of the attitude control system. This noise is significant only on the third pair of deflection plates which have the largest bias voltage. The origin of the noise is probably from variation in the capacitance to ground caused by rocket vibration. The capacitance variation creates a signal from the time derivative of CV, where C is the capacitance and V is the bias voltage. The dependence on bias voltage is consistent with the absence of noise on the collection plates with low bias voltage. The noise is a damped sinusoid at ∼100 Hz and is removed from the data by averaging data points with the Gaussian smoothing function.

C. Spurious charge generation

It has been shown that the impact of uncharged particles on the collection plates may result in the generation of charged fragments.[38–40] The charged fragments leaving the plates would create a current appearing to be from the collection of particles with the opposite sign of charge. Above the bottom plates are collection plates with +54 V bias and −54 V bias. If charge is released from the bottom plates, we expect that it would be collected by the biased plates. There is a range of altitudes (82–85 km) in the data for which there are large signals on the bottom plates with no collection by the plates with the largest bias voltage. We interpret this to indicate that the collection by the bottom plates is from negative charge collection and not from the generation of positive fragments.

D. Photoelectric currents

There is a possibility of photoelectric emission from the graphite collecting plates due to solar ultraviolet. The pair of collection plates No. 4 at the bottom of the instrument are potentially the most exposed to UV light through the venting windows. The exposure is a function of the orientation of the payload relative to the Sun. The flight signals from these electrodes show small spikes (∼0.1 nA) at the rocket rotation frequency that may be due to photoelectron emission. The spikes are out of phase for the two collection plates, which can be explained by the UV illumination of only one side of the instrument. The data show no indication of photoelectric effect from the other collectors. The two channels with the highest bias voltages have signals that return nearly to zero above the cloud layer (>88 km). The conclusion is that the photoelectric effect is not sufficiently large to significantly affect the data.

V. CONCLUSION

An electrostatic mass analyzer for aerosol particles has operated successfully on a sounding rocket in the 75–95 km region in which NLCs form in the polar summer mesosphere. The analyzer has found the charge-to-mass ratio of the cloud particles and this provides a mass analysis with low resolution, with the assumption of one unit charge per particle. This assumption is supported by charging theory for radii less than 10 nm. Particles that are larger than 10 nm may be multiply charged; thus, for the channels collecting

the largest particles, the charge number density may be larger than the particle number density. The analyzer returned data for the charge densities for particles with radii of <0.5, 0.5–1, 1–2, and >3 nm. The charged aerosol particles had previously been detected by single-channel charge-collecting instruments. The mass analyzer operated in a region with molecular number density of $\sim 10^{14}$ cm^{-3} which is higher than is customary for mass analysis of molecular ions. The disparity in mass between the aerosol particles and air molecules results in aerosol trajectories within the instrument that are less affected by collisions than the trajectories of light ions. The effect of collisions on the sensitivity of the analyzer to both light ions and heavier aerosol particles was found by numerical simulations of the aerodynamic flow and of the trajectories of the particles that included both the electrostatic force and the forces from collisions. The two flights of the instrument showed that the limited collection of electrons was consistent with a negative payload potential. The eight-channel analyzer provided for the first time simultaneous measurements of the charge density on both positive and negative aerosol particles in several ranges of size.

ACKNOWLEDGMENTS

[1] G. E. Thomas, Adv. Space Res. **14**, 101 (1994).
[2] M. Rapp, G. E. Thomas, and G. Baumgarten, J. Geophys. Res. **112**, D03211 (2007).
[3] M. Rapp and F.-J. Lübken, Atmos. Chem. Phys. **4**, 2601 (2004).
[4] D. M. Hunten, R. P. Turco, and O. B. Toon, J. Atmos. Sci. **37**, 1342 (1980).
[5] J. D. Mitchell, C. L. Croskey, and R. A. Goldberg, Geophys. Res. Lett. **28**, 1423 (2001).
[6] O. Havnes, J. Trøim, T. Blix, W. Mortensen, L. I. Næsheim, E. Thrane, and T. Tønneson, J. Geophys. Res. **101**, 10839 (1996).
[7] L. J. Gelinas, K. A. Lynch, M. C. Kelley, S. Collins, S. Baker, Q. Zhou, and J. S. Friedman, Geophys. Res. Lett. **25**, 4047 (1998).
[8] J. Gumbel and G. Witt, Geophys. Res. Lett. **25**, 493 (1998).
[9] C. L. Croskey, J. D. Mitchell, M. Friedrich, K. M. Torkar, U.-P. Hoppe, and R. A. Goldberg, Geophys. Res. Lett. **28**, 1427 (2001).
[10] M. Horányi, S. Robertson, B. Smiley, J. Gumbel, G. Witt, and B. Walch, Geophys. Res. Lett. **27**, 3825 (2000).
[11] B. Smiley, S. Robertson, M. Horányi, T. Blix, M. Rapp, R. Latteck, and J. Gumbel, J. Geophys. Res. **108**, 8444 (2003).
[12] S. Robertson, B. Smiley, M. Horányi, Z. Sternovsky, J. Gumbel, and J. Stegman, IEEE Trans. Plasma Sci. **32**, 716 (2004).
[13] B. Smiley, M. Rapp, T. A. Blix, S. Robertson, M. Horányi, R. Latteck, and J. Fiedler, J. Atmos. Sol.-Terr. Phys. **68**, 114 (2006).
[14] K. Amyx, Z. Sternovsky, S. Knappmiller, S. Robertson, M. Horányi, and J. Gumbel, J. Atmos. Sol.-Terr. Phys. **70**, 61 (2008).
[15] C. L. Croskey, J. D. Mitchell, M. Friedrich, F. J. Schmidlin, and J. W. Meriwether, Adv. Space Res. **32**, 741 (2003).
[16] M. Rapp, J. Hedin, I. Strelnikova, M. Friedrich, J. Gumbel, and F.-J. Lübken, Geophys. Res. Lett. **32**, L23821 (2005).
[17] M. Horányi, J. Gumbel, G. Witt, and S. Robertson, Geophys. Res. Lett. **26**, 1537 (1999).
[18] B. Feuerbacher and B. Fitton, J. Appl. Phys. **43**, 1563 (1972).
[19] G. A. Bird, Planet. Space Sci. **36**, 921 (1988).
[20] G. A. Bird, *Molecular Gas Dynamics and the Direct Simulation of Gas Flows* (Oxford University Press, New York, 1994).
[21] H. M. Mott-Smith and I. Langmuir, Phys. Rev. **28**, 727 (1926).
[22] K. R. MacKenzie, R. J. Taylor, D. Cohn, E. Ault, and H. Ikezi, Appl. Phys. Lett. **18**, 529 (1971).
[23] K. T. Whitby and B. Y. H. Liu, in *Aerosol Science*, edited by C. N. Davies (Academic, London, 1966), p. 59.
[24] W. H. Press, S. A. Teukolsky, W. T. Vetterling, and B. P. Flannery, *Numerical Recipes* (Cambridge University Press, Cambridge, England, 2007).
[25] F.-J. Lübken, J. Geophys. Res. **104**, 9135 (1999).
[26] S. Robertson and Z. Sternovsky, Phys. Rev. E **67**, 046405 (2003).
[27] P. S. Epstein, Phys. Rev. **23**, 710 (1924).
[28] W. D. Hayes and R. F. Probstein, *Hypersonic Flow Theory* (Academic, New York, 1959), Chap. 10.3.
[29] R. F. Probstein, *Society for Industrial and Applied Mathematics (SIAM)* (SIAM, Philadelphia, 1969) [Note to editors: SIAM seems to be both the author and publisher of this conference proceeding volume. The printer is J. W. Arrowsmith, Ltd., Bristol, England].
[30] M. C. Kelley, *The Earth's Ionosphere* (Academic, New York, 1989).
[31] Z. Sternovsky, M. Horányi, and S. Robertson, Phys. Rev. A **64**, 023203 (2001).
[32] L. A. Viehland and E. A. Mason, At. Data Nucl. Data Tables **60**, 37 (1995).
[33] M. Friedrich, K. M. Torkar, R. A. Goldberg, J. D. Mitchell, C. L. Croskey, and G. Lehmacher, Proceedings of the 13th ESA Symposium on European Rocket and Balloon Programmes and Related Research, 1997 (unpublished), ESA Paper No. SP-397, p. 381.
[34] H. P. Eubank, R. A. Peck, and R. Truell, Rev. Sci. Instrum. **25**, 989 (1954).
[35] E. Kopp, P. Eberhardt, U. Herrmann, and L. G. Björn, J. Geophys. Res. **90**, 13041 (1985).
[36] T. A. Jacobsen and M. Friedrich, J. Atmos. Terr. Phys. **41**, 1195 (1979).
[37] G. Baumgarten, J. Fiedler, and G. von Cossart, Adv. Space Res. **40**, 772 (2007).
[38] A. A. Vostrikov, D. Yu Dubov, and M. R. Predtechenskiy, Chem. Phys. Lett. **139**, 124 (1987).
[39] P. U. Andersson and J. B. C. Pettersson, Z. Phys. D: At., Mol. Clusters **41**, 57 (1997).
[40] O. Havnes and L. I. Næsheim, Ann. Geophys. **25**, 623 (2007).